



Article

Electronic Structures and Photoelectric Properties in $\text{Cs}_3\text{Sb}_2\text{X}_9$ ($\text{X} = \text{Cl}, \text{Br}, \text{or I}$) under High Pressure: A First Principles Study

Yanwen Wu ¹, Guangbiao Xiang ¹, Man Zhang ¹, Dongmei Wei ¹, Chen Cheng ^{1,*}, Jiancai Leng ² and Hong Ma ^{1,*}

¹ Shandong Provincial Key Laboratory of Optics, Photonic Device and Collaborative Innovation Center of Light Manipulations and Applications, School of Physics and Electronics, Shandong Normal University, Jinan 250014, China

² Department of Physics, School of Electronic and Information Engineering, Qilu University of Technology (Shandong Academy of Science), Jinan 250353, China

* Correspondence: drcheng@sdnu.edu.cn (C.C.); mahong@sdnu.edu.cn (H.M.)

Abstract: Lead-free perovskites of $\text{Cs}_3\text{Sb}_2\text{X}_9$ ($\text{X} = \text{Cl}, \text{Br}, \text{or I}$) have attracted wide attention owing to their low toxicity. High pressure is an effective and reversible method to tune bandgap without changing the chemical composition. Here, the structural and photoelectric properties of $\text{Cs}_3\text{Sb}_2\text{X}_9$ under high pressure were theoretically studied by using the density functional theory. The results showed that the ideal bandgap for $\text{Cs}_3\text{Sb}_2\text{X}_9$ can be achieved by applying high pressure. Moreover, it was found that the change of the bandgap is caused by the shrinkage of the Sb-X long bond in the $[\text{Sb}_2\text{X}_9]^{3-}$ polyhedra. Partial density of states indicated that Sb-5s and X-p orbitals contribute to the top of the valence band, while Sb-5p and X-p orbitals dominate the bottom of the conduction band. Moreover, the band structure and density of states showed significant metallicity at 38.75, 24.05 GPa for $\text{Cs}_3\text{Sb}_2\text{Br}_9$ and $\text{Cs}_3\text{Sb}_2\text{I}_9$, respectively. Moreover, the absorption spectra showed the absorption edge redshifted, and the absorption coefficient of the $\text{Cs}_3\text{Sb}_2\text{X}_9$ increased under high pressure. According to our calculated results, the narrow bandgap and enhanced absorption ability under high pressure provide a new idea for the design of the photovoltaic and photoelectric devices.

Keywords: $\text{Cs}_3\text{Sb}_2\text{Br}_9$; the first principles; high pressure; band structures; photoelectric properties



Citation: Wu, Y.; Xiang, G.; Zhang, M.; Wei, D.; Cheng, C.; Leng, J.; Ma, H. Electronic Structures and Photoelectric Properties in $\text{Cs}_3\text{Sb}_2\text{X}_9$ ($\text{X} = \text{Cl}, \text{Br}, \text{or I}$) under High Pressure: A First Principles Study.

Nanomaterials **2022**, *12*, 2982. <https://doi.org/10.3390/nano12172982>

Academic Editor: Cesare Malagù

Received: 18 July 2022

Accepted: 26 August 2022

Published: 29 August 2022

Publisher's Note: MDPI stays neutral with regard to jurisdictional claims in published maps and institutional affiliations.



Copyright: © 2022 by the authors. Licensee MDPI, Basel, Switzerland. This article is an open access article distributed under the terms and conditions of the Creative Commons Attribution (CC BY) license (<https://creativecommons.org/licenses/by/4.0/>).

1. Introduction

In recent years, halide perovskites have received a great amount of attention because of their excellent performances in photoelectric and photovoltaic applications [1–3], such as, lasers, light emitting diodes (LED), solar cell, and photocatalysis [4–6]. Lead halide perovskites are typical representatives due to their excellent performances. However, it is well known that lead halide perovskites suffer from low stability and high toxicity of lead in the development and applications [2,7]. Therefore, to solve the problem of toxicity, lead-free perovskites have attracted more and more attention. Since Sb^{3+} has a similar electronic structure and ionic radius as Pb^{2+} , it exhibits lower toxicity and better chemical stability than the neighboring heavy metals Pb^{2+} . Thus, $\text{Cs}_3\text{Sb}_2\text{X}_9$ ($\text{X} = \text{Cl}, \text{Br}, \text{or I}$) becomes a superior candidate for low-toxicity polymer solar cells (PSCs) [8]. $\text{Cs}_3\text{Sb}_2\text{I}_9$ microplates were already synthesized by the two-step chemical vapor deposition process and demonstrated superior thermal stability within a wide temperature range from 80 K to 380 K [9]. Arto Hiltunen et al. found that the average power conversion efficiency (PCE) doubled by using P3HT (poly(3-hexylthiophene-2,5-diyl)) as a hole transport material for a $\text{Cs}_3\text{Sb}_2\text{I}_9$ solar cell with a PCE of 2.5%. The signal did not diminish during the storage for 1 month [10]. $\text{Cs}_3\text{Sb}_2\text{Br}_9$ was first proposed as an absorber layer in PSCs to absorb solar energy by Sachchidanand et al. A maximum PCE of 15.69% for PSCs with this absorber layer was already reported [11]. The first LED with $\text{Cs}_3\text{Sb}_2\text{I}_9$ fabricated by the vapor-anion exchange method as an emitter were reported by Anupriya Singh et al. The $\text{Cs}_3\text{Sb}_2\text{I}_9$ film obtained by this method had exhibited wide photoluminescence spectrum with a

full width at half maximum of 120 nm. Visible-infrared radiance of $0.012 \text{ W} \cdot \text{Sr}^{-1} \cdot \text{m}^{-2}$ at 6 V was measured in electroluminescent devices with $\text{Cs}_3\text{Sb}_2\text{I}_9$ as the emitter layer [12]. Umami Kalsom Noor Din et al. also synthesized lead-free, fully inorganic single crystal perovskite $\text{Cs}_3\text{Sb}_2\text{Br}_9$ with a photoluminescence quantum yield of 23% using an inverse temperature crystallization method [13]. These excellent works have confirmed that lead-free perovskites have a promising future in the photovoltaic and photoelectronic fields.

According to the Shockley-Queisser limit, the optimal bandgap energy for photovoltaic material is 1.3–1.5 eV [14]. There are few materials that naturally conform to the ideal bandgap. The reason of low PCE for a Sb-based solar cell is that the bandgap is too large. Because of the advantage that perovskite is extremely flexible and the bandgap can be adjusted to achieve the ideal value, previous works have already reported that the absorption spectra and bandgaps (from ~1.9 to ~3.1 eV) of the $\text{A}_3\text{B}_2\text{X}_9$ ($\text{A} = \text{Cs}, \text{MA}, \text{FA}$; $\text{B} = \text{As}, \text{Sb}, \text{Bi}$; and $\text{X} = \text{Cl}, \text{Br}, \text{I}$) material could be changed by atomic substitution [15]. In addition, doping is also an effective method to change the ideal bandgap. The various concentrations of Ru^{3+} were doped into $\text{Cs}_3\text{Bi}_2\text{I}_9$ by atomic substitution of Bi^{3+} to adjust its bandgap and optical properties. A corresponding reduction in bandgap occurs with the doping concentration of Ru^{3+} . When the doping concentration is 5%, the bandgap of $\text{Cs}_3\text{Bi}_{1.9}\text{Ru}_{0.1}\text{I}_9$ reduced from 2.2 to 1.80 eV. The narrowing of the bandgap expands its applications in photoelectronic and photovoltaic fields [16]. High pressure can also adjust the crystal structures and physical properties without changing the chemical composition. The most important advantage of high pressure is that high pressure is reversible. Namely, when the pressure is released, the material can return to its original properties [17]. Guang Dai et al. found that the emission peak of CsPbBr_3 perovskite quantum dots could be modulated by the applied external pressure. Detailed analysis showed that the wavelength shifting was correlated to the external pressure with a good linear relationship. They demonstrated novel perovskite quantum dots based on optical a Fabry-Perot (FP) pressure sensor for the first time [18]. Ting Geng et al. successfully narrowed the bandgap of lead-free perovskite $\text{Cs}_3\text{Sb}_2\text{I}_9$ nanocrystals from 2.05 to 1.36 eV at 20 GPa pressure, with a measurable rate of 33.7%. The change in bandgap can be attributed to the pressure-induced compression and distortion of the lattice [19]. Experimental results obtained by Lianwei Wu et al. had reported that $\text{Cs}_3\text{Sb}_2\text{I}_9$ can reach a bandgap of 1.32 eV at 20 GPa, successfully obtaining the ideal semiconductor bandgap (1.34 eV). As the pressure continues to increase, this material also exhibited metallic properties [17]. Therefore, high pressure can effectively adjust the structural and photoelectronic properties of perovskite materials.

Although so many theoretical and experimental works already reported, there is still a lack of systematic theoretical calculation for band structures and photoelectronic properties of $\text{Cs}_3\text{Sb}_2\text{X}_9$ ($\text{X} = \text{Cl}, \text{Br}, \text{or I}$) under high pressure. In the present work, we systematically investigated the electronic structures and optical properties of $\text{Cs}_3\text{Sb}_2\text{X}_9$ ($\text{X} = \text{Cl}, \text{Br}, \text{or I}$) under high pressure from 0 to 40 GPa by Density Functional Theory (DFT). Firstly, the structural properties and bandgap of $\text{Cs}_3\text{Sb}_2\text{X}_9$ at high pressure was calculated. Then, the changes of lattice parameter and bond length under high pressure were investigated. Finally, the density of states and optical properties under high pressure were calculated. The findings in this article are expected to provide insights into the physical and chemical properties of $\text{Cs}_3\text{Sb}_2\text{X}_9$ under high pressure and a helpful guide to develop the efficient photoelectronic and photovoltaic applications.

2. Computational Model and Method

The research in this paper is based on the quantum mechanical approach of DFT. DFT is often referred to as first-principles computations. The DFT calculations were performed using the projector-augmented wave (PAW) method [20], implemented in Vienna Ab-initio Simulation Package [21,22]. A single point at the generalized gradient approximation (GGA) of Perdew-Burke-Ernzerh (PBE) was used for obtaining the optimized lattice parameter, atomic position, density of state and electronic band structure [23]. On the one hand, DFT can provide microscopic explanations for experimental phenomena and identify the

essential reasons of the phenomena. On the other hand, it can also predict the properties of new materials and thus provide theoretical guidance for the design of new experiments and the selection of materials for specific properties.

The layered form of $\text{Cs}_3\text{Sb}_2\text{X}_9$ is more suitable for photovoltaic applications than the dimeric form [24]. Therefore, all calculations were chosen in layered form. The initial structure was downloaded from the Crystallography Open Database and further optimized in VASP [25–27]. In order to determine optical properties for $\text{Cs}_3\text{Sb}_2\text{X}_9$, both the HSE06 hybrid exchange-correlation functional and PBE algorithms were used. We adjusted the PSTRESS in the INCAR file to change the pressure value in optimizations of the structure. The kinetic cut-off energy for the plane wave expansion was taken to be 500 eV. The structural optimizations were stopped when all the total forces on each atom were below 0.01 eV/Å. The convergence criterion for the energy was set to be 10^{-6} eV [28]. The $5 \times 5 \times 5$ k-point grid was applied to structure optimization and HSE calculated optical properties, while the dense $18 \times 18 \times 18$ grid was applied to the PBE algorithm for calculated optical properties. To make the density of states seem smooth, $16 \times 16 \times 16$ k-point was used for the calculations. The high-symmetry points for the band structure were taken as Γ (0 0 0), M (0.5 0 0), K (0.33 0.33 0), Γ (0 0 0), A (0 0 0.5), L (0.5 0 0.5), H (0.33 0.33 0.5) and A (0 0 0.5), respectively [24]. The crystal structures were visualized using VESTA [29].

3. Results and Discussion

$\text{Cs}_3\text{Sb}_2\text{X}_9$ belongs to the trigonal crystal structure with the space group $P3(-)m1$ (no.164). Figure 1a, b showed the optimized crystal structure of the $\text{Cs}_3\text{Sb}_2\text{X}_9$. $\text{Cs}_3\text{Sb}_2\text{X}_9$ is composed of two $[\text{Sb}_2\text{X}_9]^{3-}$ polyhedra in a single unit, with the two Sb^{3+} ions located on the body diagonal of the unit cell and eight top corners occupied by Cs^+ . These connected $[\text{Sb}_2\text{X}_9]^{3-}$ polyhedra of the bilayer are stacked together. $\text{Cs}_3\text{Sb}_2\text{X}_9$ is considered as layered material (Figure 1c) and exhibits triangular symmetry [28]. The optimized atomic coordinates without high pressure are listed in Supplementary Materials Table S1. In order to indicate that the structures are still stable under pressure, we calculated the pressure-dependent Gibbs free energy and show it in Supplementary Materials Figure S1.

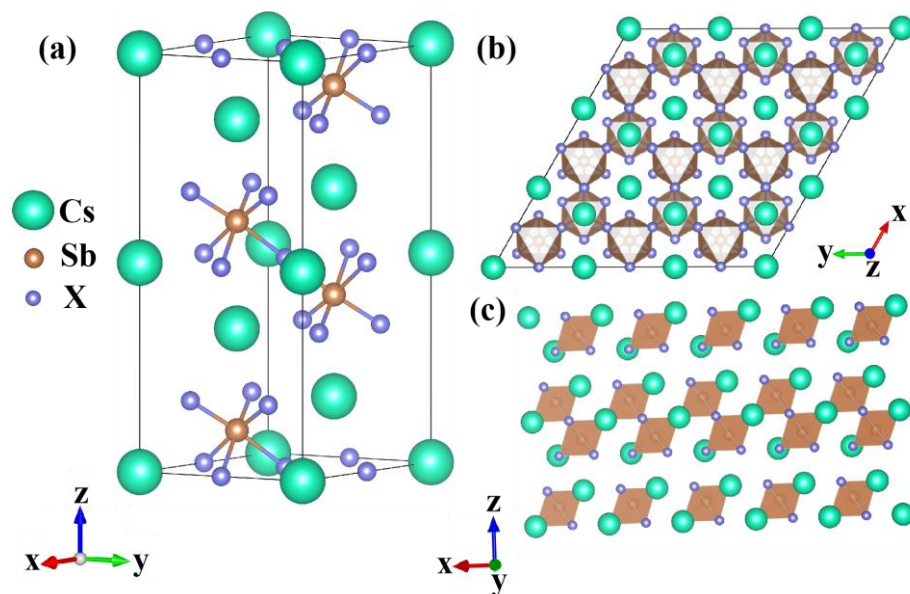


Figure 1. (a) Optimized structure of $\text{Cs}_3\text{Sb}_2\text{X}_9$; (b) corresponding crystal structure of $\text{Cs}_3\text{Sb}_2\text{X}_9$ viewed in the xy plane; (c) layered form $\text{Cs}_3\text{Sb}_2\text{X}_9$.

The previous and present theoretical values of lattice parameters a , b and c bandgap energy E_g for $\text{Cs}_3\text{Sb}_2\text{X}_9$ are presented in Table 1. According to Table 1, the PBE optimized lattice parameters are in good agreement with the previously reported and experimental

values. For example, the lattice parameters of $\text{Cs}_3\text{Sb}_2\text{Cl}_9$ are 7.817, 7.817 and 9.494 Å obtained in this work, which are very close to the reported theoretical values of 7.827, 7.827 and 9.472 Å and slightly larger than those of the experimental values. As the atomic number increases from Cl to I, the lattice parameter increases in turn. In addition, the ionic radii of Cl^- , Br^- , and I^- are 1.81, 1.96 and 2.20 Å, respectively, which showed similar behavior as the lattice parameters [28]. Moreover, the bandgap energies calculated by PBE are 2.40, 2.01 and 1.55 eV without pressure for $\text{Cs}_3\text{Sb}_2\text{Cl}_9$, $\text{Cs}_3\text{Sb}_2\text{Br}_9$ and $\text{Cs}_3\text{Sb}_2\text{I}_9$, respectively. Compared to the reported theoretical and experimental values, the bandgap energies calculated by PBE are small [30].

Table 1. Calculated results (Present), previous theoretical (Pre) and experimental (Exp) values of lattice parameters a, b, and c (Å), bandgap energy E_g (eV) of $\text{Cs}_3\text{Sb}_2\text{X}_9$.

Species		a	b	c	E_g
$\text{Cs}_3\text{Sb}_2\text{Cl}_9$	Present	7.817	7.817	9.494	2.40
	Pre.	7.827 [28]	7.827 [28]	9.472 [28]	2.41 [31,32]
	Exp.	7.633 [28]	7.633 [28]	9.345 [28]	3.09 [28]
$\text{Cs}_3\text{Sb}_2\text{Br}_9$	Present	8.137	8.137	9.969	2.01
	Pre.	8.138 [28]	8.138 [28]	9.943 [28]	2.60(HSE) [28]
	Exp.	7.930 [28]	7.930 [28]	9.716 [28]	2.30 [28]
$\text{Cs}_3\text{Sb}_2\text{I}_9$	Present	8.678	8.678	10.614	1.55
	Pre.	8.661 [33]	8.661 [33]	10.625 [33]	1.55 [33]
	Exp.	8.420 [33]	8.420 [33]	10.386 [33]	2.05 [27,33]

The photoelectric properties of the materials are closely related with their band structures. Therefore, we calculated the band structures of $\text{Cs}_3\text{Sb}_2\text{X}_9$ under the pressure from 0 to 40 GPa. Figure 2a–d show the band structures of $\text{Cs}_3\text{Sb}_2\text{I}_9$ under the pressure of 0, 10, 20 and 40 GPa. As the pressure increases, the bandgap of $\text{Cs}_3\text{Sb}_2\text{I}_9$ decreases. The bandgap under the pressure of 0, 10, 20 and 40 GPa are 1.55, 0.63, 0.17 and -0.54 eV, respectively. According to Figure 2a, $\text{Cs}_3\text{Sb}_2\text{I}_9$ is a direct bandgap structure without pressure, with both the conduction band minimum (CBM) and the valence band maximum (VBM) at point Γ [28]. In addition, the CBM still remains at point Γ , while the VBM moves towards point K under the high pressure. The shift of the high symmetry points from Γ to the K point also appeared in the calculation of the energy band of CsYbCl_3 at high pressure (160 GPa) [34]. As shown in Figure 2e, the valence band consists of Sb-5s and I-5p, and the conduction band mainly consists of Sb-5p and I-5p when no pressure is applied. Figure 2f shows that at a pressure of 40 GPa, the valence band still consists of Sb-5s and I-5p, while the conduction band is dominated by Sb-5p, I-5p and I-4d. The interaction between the I and Sb orbitals leads to a change in the high symmetry point of the energy band. The inter-conversion of direct and indirect bandgap owing to the change in composition has also been reported previously [35]. The band structures of $\text{Cs}_3\text{Sb}_2\text{Cl}_9$ and $\text{Cs}_3\text{Sb}_2\text{Br}_9$ under pressure are shown in Supplement Figures S2 and S3. $\text{Cs}_3\text{Sb}_2\text{Br}_9$ is also a direct bandgap semiconductor without pressure with both CBM and VBM at point Γ , which is similar as that of $\text{Cs}_3\text{Sb}_2\text{I}_9$. However, $\text{Cs}_3\text{Sb}_2\text{Cl}_9$ exhibits an indirect bandgap with CBM at point A and VBM at point Γ when the pressure is not applied [24]. The CBM shifts towards point Γ , and the VBM starts moving from point Γ to point K under the pressure, still maintaining the indirect bandgap. Based on Supplement Figures S2 and S3, the bandgap energies are 2.4, 1.74, 1.28 and 0.54 eV for $\text{Cs}_3\text{Sb}_2\text{Cl}_9$ and 2.00, 1.16, 0.70 and -0.04 eV for $\text{Cs}_3\text{Sb}_2\text{Br}_9$ under the pressures of 0, 10, 20 and 40 GPa, respectively. The Fermi level is at 0 eV, as shown by a red horizontal dashed line. The locations of the VBM are -0.078 , -0.051 , -0.021 and 0.308 eV, while the position of the CBM is 1.48, 0.58, 0.15 and -0.23 eV for $\text{Cs}_3\text{Sb}_2\text{I}_9$. The conduction band and valence band gradually move to the Fermi energy level and then

overlap with each other, indicating that the material presents metallic properties [19,20]. According to Supplementary Materials Figures S2 and S3, $\text{Cs}_3\text{Sb}_2\text{I}_9$ and $\text{Cs}_3\text{Sb}_2\text{Cl}_9$ also exhibit significant metallicity at 24.05 and 38.75 GPa. Therefore, it is possible to obtain the desired bandgap energy by tuning the pressure.

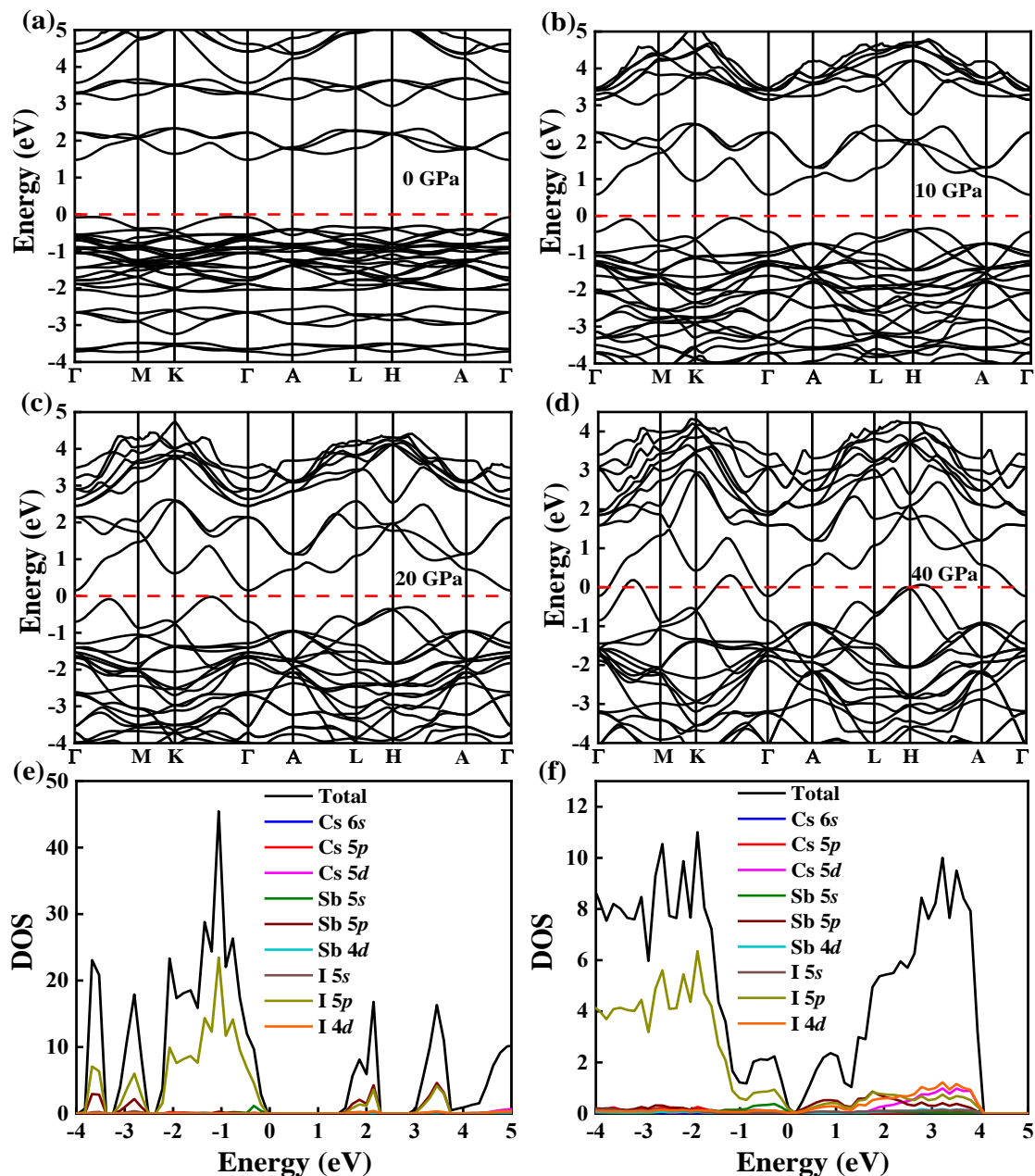


Figure 2. Band structures of $\text{Cs}_3\text{Sb}_2\text{I}_9$ under different pressures of 0 (a); 10 (b); 20 (c); 40 GPa (d). The red dashed line is a guide line at 0. Total and partial density of states for $\text{Cs}_3\text{Sb}_2\text{I}_9$ without (e) and with (f) pressure calculated by PBE functional.

It is noted that the bandgap calculated by PBE is smaller than that measured by the experiment. According to a previous study, the ideal bandgap of $\text{Cs}_3\text{Sb}_2\text{I}_9$, namely 1.36 eV, was achieved under a pressure of 20 GPa [19]. Because the PBE calculation underestimates the bandgap value, the bandgap calculated in this work is only 0.17 eV at 20 GPa. According to our calculated results, $\text{Cs}_3\text{Sb}_2\text{X}_9$ ($\text{X} = \text{Cl}, \text{Br}, \text{I}$) reaches ideal bandgap values (1.34 eV) at 19.02, 6.82 and 1.14 GPa, respectively. The more theoretical values of the

bandgap energies under pressure for $\text{Cs}_3\text{Sb}_2\text{Cl}_9$, $\text{Cs}_3\text{Sb}_2\text{Br}_9$ and $\text{Cs}_3\text{Sb}_2\text{I}_9$ are listed in Supplementary Materials Tables S2–S4.

Figure 3a–c showed the calculated lattice parameters of $\text{Cs}_3\text{Sb}_2\text{X}_9$ under pressure. All lattice parameters displayed a decreasing trend when the pressure increased. Since $\text{Cs}_3\text{Sb}_2\text{X}_9$ is a trigonal crystal structure, the lattice constants of the a and b are equal. Lattice constants for a and b varied in the range 7.82–6.31, 8.14–7.73 and 8.68–6.99 Å for $\text{Cs}_3\text{Sb}_2\text{Cl}_9$, $\text{Cs}_3\text{Sb}_2\text{Br}_9$ and $\text{Cs}_3\text{Sb}_2\text{I}_9$, respectively. In contrast, the lattice constant in the c-direction decreases from 9.49 to 7.77 Å, 9.97 to 8.05 Å and 10.61 to 8.43 Å for $\text{Cs}_3\text{Sb}_2\text{Cl}_9$, $\text{Cs}_3\text{Sb}_2\text{Br}_9$ and $\text{Cs}_3\text{Sb}_2\text{I}_9$, respectively. The decrease in lattice constant indicated that the continuous pressure induced a contraction of the unit cell. S. Idrissi et al. reported that the changes in the lattice constant cause a shrinkage in the bandgap energies [36]. Both lattice constants and bandgaps calculated in this paper for $\text{Cs}_3\text{Sb}_2\text{X}_9$ had the same variation trend. Figure 3d showed the change in unit cell volume, which indicated that the volume of $\text{Cs}_3\text{Sb}_2\text{X}_9$ gradually decrease. As the pressure increases, the interatomic distance decreases, leading to gradual shrinkage in both lattice constant and unit cell volume [36]. This trend follows the similar behavior as the change in lattice constants, decreasing rapidly at first and then gradually slowing down. The reason is that as the space between atoms decreases, the repulsive forces between atoms become stronger, resulting in more difficult to compress [37].

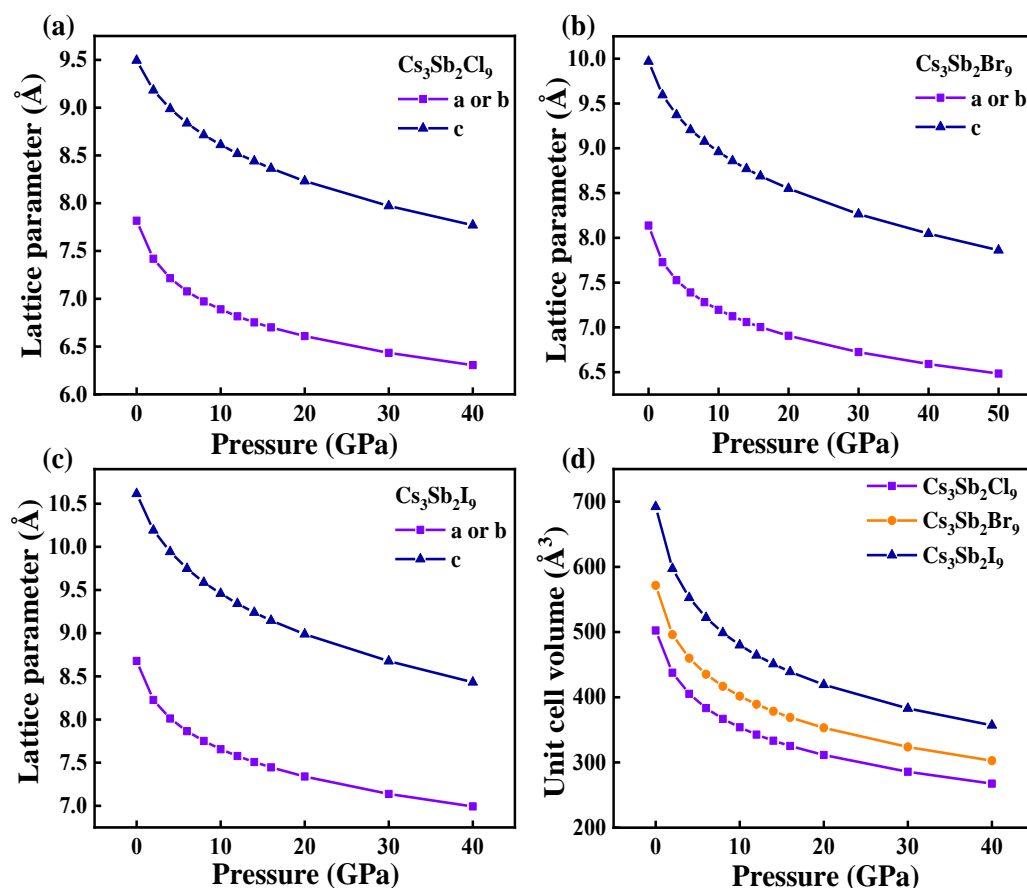


Figure 3. Calculated lattice parameter a, b and c of $\text{Cs}_3\text{Sb}_2\text{Cl}_9$ (a); $\text{Cs}_3\text{Sb}_2\text{Br}_9$ (b); $\text{Cs}_3\text{Sb}_2\text{I}_9$ (c); as a function of pressure: (d) lattice volume of $\text{Cs}_3\text{Sb}_2\text{X}_9$ with increasing pressure from 0 to 40 GPa.

To explain the shrinking bandgap and lattice constant of the $\text{Cs}_3\text{Sb}_2\text{X}_9$ under pressure, we also calculated the relation between the bond length and the pressure. As shown in Figure 4a, two different bond lengths, L_1 and L_2 , are defined as the short and long Sb-X bonds, respectively. The bond lengths were obtained using the VESTA. Figure 4b–d presented bond length as a function of pressure for $\text{Cs}_3\text{Sb}_2\text{X}_9$. The bond lengths of

$\text{Cs}_3\text{Sb}_2\text{Cl}_9$, $\text{Cs}_3\text{Sb}_2\text{Br}_9$ and $\text{Cs}_3\text{Sb}_2\text{I}_9$ increase in order without pressure, which can be explained by the increase in the atomic radius of halogen atoms [28]. Both short and long Sb-X bond lengths decrease with pressure, indicating that $\text{Cs}_3\text{Sb}_2\text{X}_9$ are compressed under the pressure. The variation range in short bond L_1 of the $\text{Cs}_3\text{Sb}_2\text{X}_9$ is 2.53–2.34, 2.69–2.44 and 2.92–2.56 Å, respectively. The long bond L_2 varies in the range of 2.84–2.45, 2.98–2.54 and 3.18–2.66 Å, respectively. The theoretically calculated bond lengths of $\text{Cs}_3\text{Sb}_2\text{X}_9$ under the pressure from 0–40 GPa are shown in Supplementary Materials Table S5. The previous work also showed that the electronic structure of $\text{Cs}_3\text{Sb}_2\text{X}_9$ was strongly affected by the Sb-X bond length [19,38]. In addition, L_1 and L_2 rapidly decrease at first and then slowly, which means that the increasing proximity of adjacent $[\text{Sb}_2\text{X}_9]^{3-}$ polyhedra leads to electrostatic interactions becoming strong under high pressure [19]. As the pressure increases, the Sb and X orbitals gradually overlap, and the electronic band dispersion increases as the Sb-X bond contracts. As a result, the CBM gradually decreases towards the Fermi energy level, and the VBM starts to rise simultaneously [17]. As a result, the narrowing of the bandgap at high pressure is presented. Combined with the above analysis, the reduction in bond length leads to a shrinkage in the lattice constant and further reduces the bandgap.

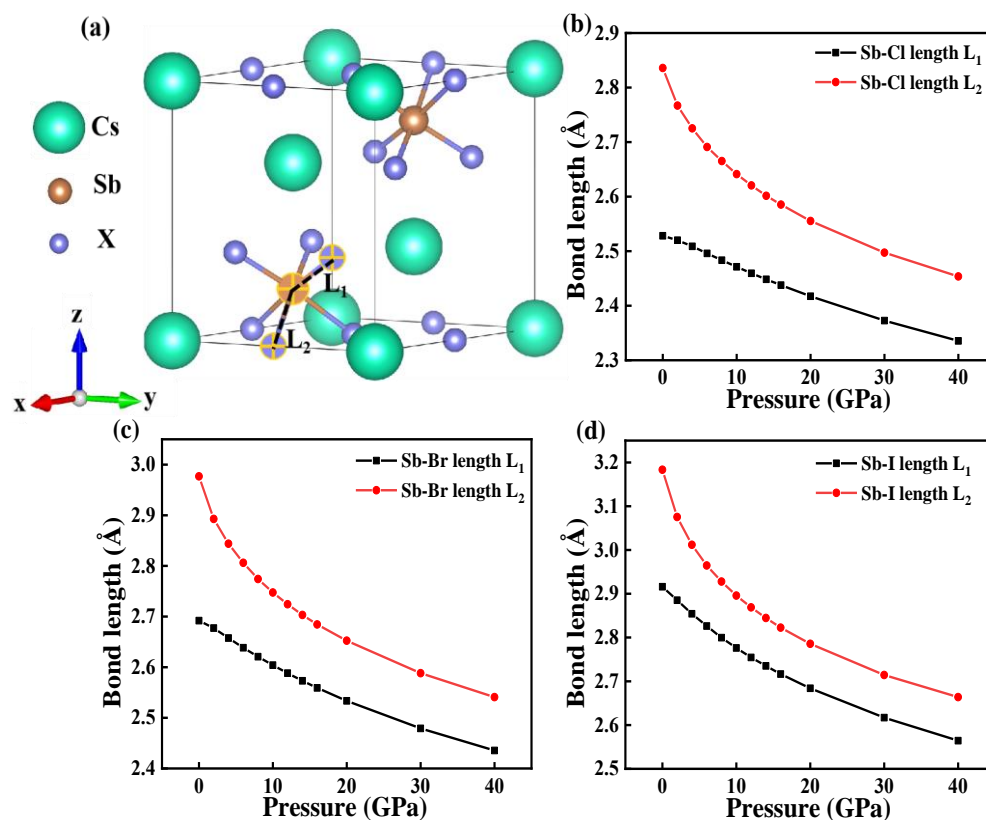


Figure 4. (a) Two types of Sb-X bonds L_1 and L_2 . Calculated bond length as a function of pressure for $\text{Cs}_3\text{Sb}_2\text{Cl}_9$ (b); $\text{Cs}_3\text{Sb}_2\text{Br}_9$ (c); and $\text{Cs}_3\text{Sb}_2\text{I}_9$ (d); as a function of pressure.

The density of states (DOS) represents the number of electrons in the unit energy range. Much information can be obtained from a DOS diagram, such as VBM, CBM and the contribution of each orbital to the total density of states. Therefore, we calculated DOS of $\text{Cs}_3\text{Sb}_2\text{X}_9$ with and without pressure to help us further understand the band structures. Here, the electronic configurations of $5s^25p^66s$ for Cs, $5s^25p^3$ for Sb, $3s^23p^5$ for Cl, $4s^24p^5$ for Br and $5s^25p^5$ for I are considered as valence electrons. As shown in Figure 5a–c, the partial density of states (DOS) indicates that the VBM of the $\text{Cs}_3\text{Sb}_2\text{X}_9$ mainly originates from Sb-5s and X-p, while the CBM is dominated by both Sb-5p and X-p. DFT analysis indicates that these results are consistent with the previous reports [28]. Figure 5d–f showed the total density of states under different pressures. As the pressure increases, both VBM

and CBM move towards the Fermi energy level and eventually overlap (for Cs₃Sb₂Br₉ and Cs₃Sb₂I₉). When the valence and conduction bands become overlapped, the material changes from semiconductor to metal, which is consistent with the previous work [39]. Additionally, according to Figure 2a-d, the conduction band dropped by 1.71 eV and the valence band rose by 0.386 eV for Cs₃Sb₂I₉. Thus, the conduction band plays a major role in the narrowing of the bandgap. The electrons that make up the conduction band are mainly provided by Sb-5p and X-p and the strong anti-bonding interaction between the two electrons [17].

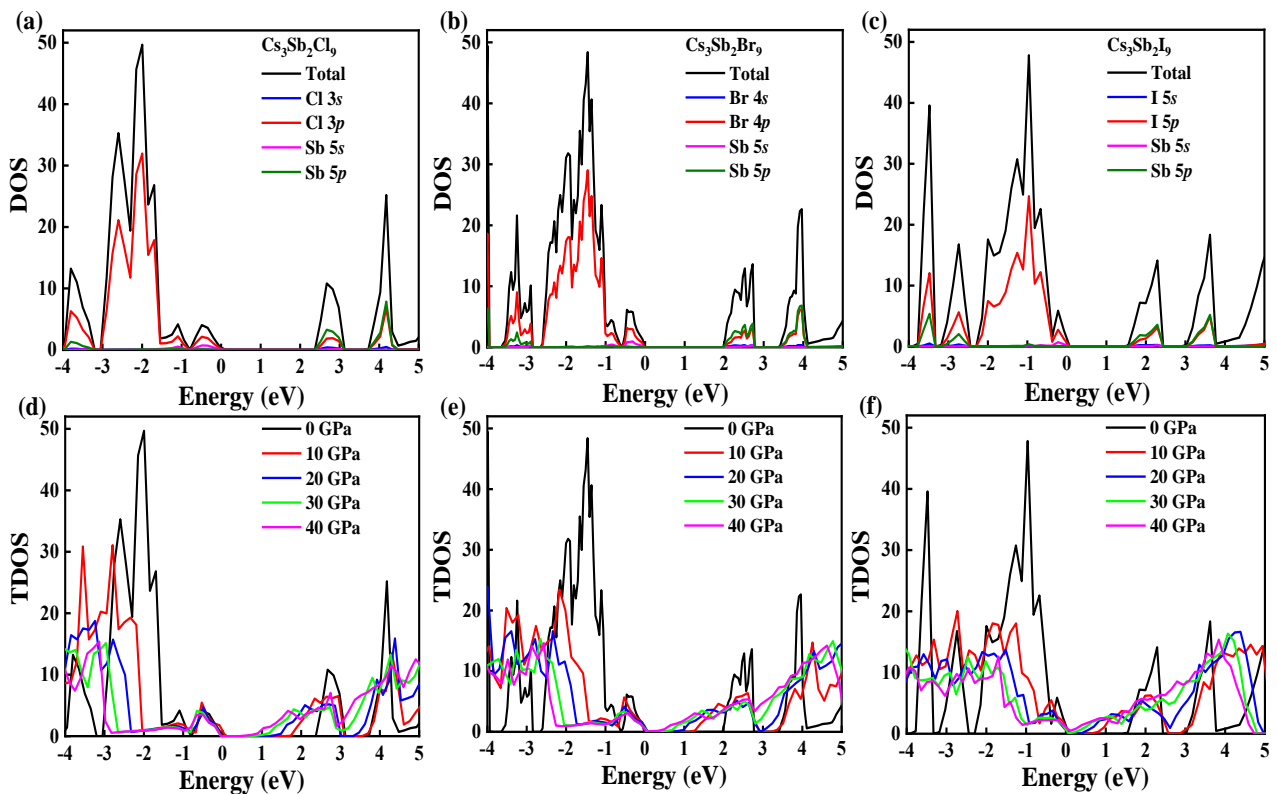


Figure 5. Total and partial density of states for Cs₃Sb₂Cl₉ (a); Cs₃Sb₂Br₉ (b); and Cs₃Sb₂I₉ (c); are calculated by PBE functional. Total density of states of Cs₃Sb₂Cl₉ (d); Cs₃Sb₂Br₉ (e); and Cs₃Sb₂I₉ (f); under different pressures.

The absorption coefficient of perovskite is significant for photoelectric and photovoltaic applications, such as solar cells, lasers and detectors. The optical absorption coefficient of perovskite is usually expressed by the complex dielectric function, i.e., $\varepsilon(\omega) = \varepsilon_1(\omega) + i\varepsilon_2(\omega)$, where ω is the frequency of the incident light and $\varepsilon_1(\omega)$ and $\varepsilon_2(\omega)$ are the real and imaginary parts of the complex dielectric function, respectively. Generally, $\varepsilon_1(\omega)$ and $\varepsilon_2(\omega)$ are used to describe the refractive and absorption behavior, respectively, which are given by the following equations [39,40]:

$$\varepsilon_1(\omega) = 1 + \frac{2}{\pi} P \int_0^{\infty} \frac{\varepsilon_2(\omega') \omega' d\omega'}{\omega'^2 - \omega^2}, \varepsilon_2(\omega) = \frac{Ve^2}{2\pi\hbar m^2 \omega^2} \int d^3k \sum_{nn'} |\langle kn|p|kn' \rangle|^2 f(kn) * (1 - f(kn')) \delta(E_{kn} - E_{kn'} - \hbar\omega) \quad (1)$$

where P is the principal value of the integral, V represents a unit volume, e is the electron charge, p represents the momentum transition matrix, and kn and kn' are the wave functions of the conduction band and valence band, respectively. The absorption coefficient, α , can be obtained by calculating the real and imaginary parts of the dielectric function [40]:

$$\alpha = 2\omega \left[\frac{(\varepsilon_1^2(\omega) + \varepsilon_2^2(\omega))^{1/2} - \varepsilon_1(\omega)}{2} \right]^{1/2}, \quad (2)$$

The high pressure influences the band structure, bandgap energy and the nature of the bonding of the band structure; these changes will further influence the optical absorption of $\text{Cs}_3\text{Sb}_2\text{X}_9$. Figure 6a–c showed the absorption spectra of $\text{Cs}_3\text{Sb}_2\text{X}_9$ as a function of photon energy at different pressures. One can see that the absorption edge shifts towards lower energies (redshift) with increasing the pressure, which is consistent with the variation of the bandgap under the pressure shown in Figure 2. The redshift of the absorption edge for CsSnCl_3 with increasing pressure was also mentioned in a previous report by Jakiul Islam et al. [37]. Supplementary Materials Figure S3 showed the optical properties calculated using the HSE06 hybrid exchange-correlation function and employing a dense $5 \times 5 \times 5$ k-point grid. The same variation trend is obtained for both PBE and HSE06. As the pressure increases, the gap between the conduction band and the valence band decreases or even overlaps, which facilitates the transport of carriers and thus enhances light absorption. In Figure 6a, the absorption peaks of $\text{Cs}_3\text{Sb}_2\text{Cl}_9$ are concentrated in the ultraviolet region and can theoretically be used as an alternative material for sterilizing surgical equipment [41], whereas in Figure 6c, the absorption spectra of $\text{Cs}_3\text{Sb}_2\text{I}_9$ fully covered the visible region and can be used in the field of solar cells [42].

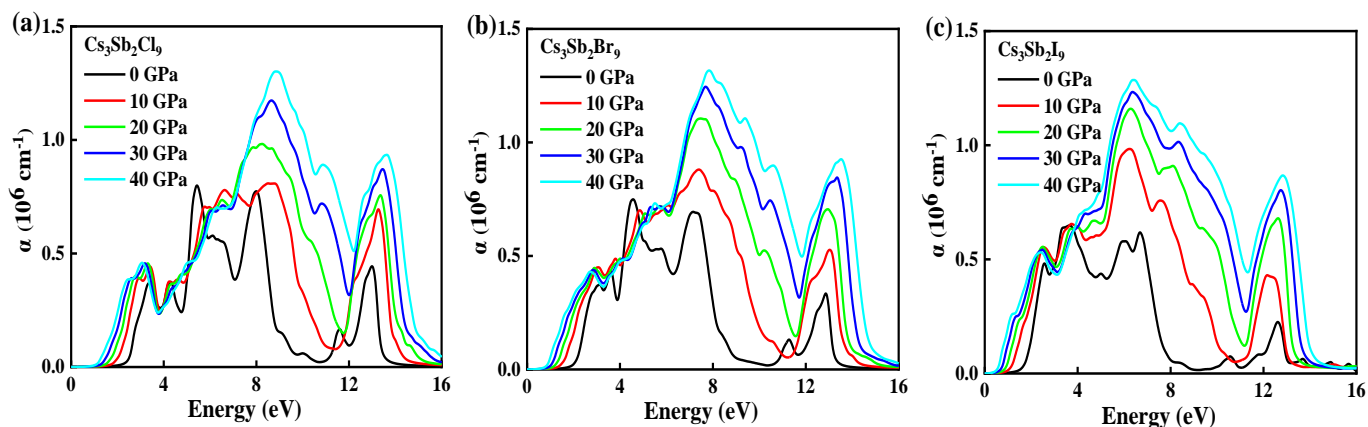


Figure 6. Optical spectra of $\text{Cs}_3\text{Sb}_2\text{Cl}_9$ (a); $\text{Cs}_3\text{Sb}_2\text{Br}_9$ (b); and $\text{Cs}_3\text{Sb}_2\text{I}_9$ (c); as a function of energy are calculated by PBE functional under different pressures.

The integral values of light absorption are shown in Table 2. The integral value for the absorption spectra gradually increases with the pressure. Supplement Table S6 shows the integral value of the absorption coefficient calculated using HSE06 algorithms, and the same regularity is obtained for both algorithms, which indicates that the pressure is beneficial for light absorption. As the pressure increases, the bandgap gradually decreases and approaches the ideal bandgap value, resulting in an increase in the light absorption of the material. Therefore, pressure can be used as an efficient and unpolluted method to adjust bandgap energies and enhance the absorption coefficient of $\text{Cs}_3\text{Sb}_2\text{X}_9$ in order to develop its applications, such as solar cells, LEDs, lasers and other photovoltaic devices.

Table 2. The calculated integral value of the absorption coefficient of the $\text{Cs}_3\text{Sb}_2\text{X}_9$ under the pressure from 0 to 40 GPa.

Pressure (GPa)	$\text{Cs}_3\text{Sb}_2\text{Cl}_9$	$\text{Cs}_3\text{Sb}_2\text{Br}_9$	$\text{Cs}_3\text{Sb}_2\text{I}_9$
0	0.70×10^6	1.21×10^6	1.50×10^6
10	0.95×10^6	1.40×10^6	1.85×10^6
20	1.04×10^6	1.44×10^6	1.95×10^6
30	1.10×10^6	1.49×10^6	2.04×10^6
40	1.15×10^6	1.54×10^6	2.14×10^6

4. Conclusions

To summarize, we have systematically investigated the electronic structure, DOS and optical properties of lead-free $\text{Cs}_3\text{Sb}_2\text{X}_9$ ($\text{X} = \text{Cl}, \text{Br}, \text{and I}$) under high pressure. Both bandgap energy and bond length of Sb-X rapidly decreased at first and then became slow with the pressure, which was led by the enhancement of the interactions of the atoms. The strong anti-bonding between $\text{Sb-5}p$ and $\text{X-}p$ caused a substantial downward shift of the conduction band and a slight upward shift of the valence band, resulting in a reduction or disappearance of the bandgap. The bandgap of $\text{Cs}_3\text{Sb}_2\text{I}_9$ can be adjusted in the range of 1.55 to -0.20 eV under pressure from 0 to 40 GPa. In addition, DOS showed that the VBM of $\text{Cs}_3\text{Sb}_2\text{X}_9$ was dominated by $\text{Sb-5}p$ and $\text{Cl-3}p$, $\text{Br-4}p$ and $\text{I-5}p$ states, and the CBM originated from $\text{Sb-5}p$ and $\text{X-}p$ states. Moreover, it was found that as the pressure increases, the absorption edge shifts towards lower energy, and the light absorption coefficient increases, which is consistent with the decrease of the bandgap energy. Therefore, the high-pressure treatment can reversibly tune the bandgap and optical properties of $\text{Cs}_3\text{Sb}_2\text{X}_9$, providing a new method for the design of the photovoltaic and photoelectronic devices.

Supplementary Materials: The following are available online at <https://www.mdpi.com/article/10.3390/nano12172982/s1>, Table S1: Optimized the atomic coordinates without high pressure. Figure S1: Calculated Gibbs free energy as a function of pressure. Figure S2: Electronic structures of $\text{Cs}_3\text{Sb}_2\text{Cl}_9$ under different pressures of 0 (a), 10 (b), 20 (c), 40 GPa (d); Figure S3: Electronic structures of $\text{Cs}_3\text{Sb}_2\text{Br}_9$ under different pressures of 0 (a), 10 (b), 20 (c), 40 GPa (d); Table S2: Calculated lattice parameters a , b , c , and bandgap energy E_g of $\text{Cs}_3\text{Sb}_2\text{Cl}_9$; Table S3: Calculated lattice parameters a , b , c , and bandgap energy E_g of $\text{Cs}_3\text{Sb}_2\text{Br}_9$; Table S4: Calculated lattice parameters a , b , c , and bandgap energy E_g of $\text{Cs}_3\text{Sb}_2\text{I}_9$; Table S5: Calculated bond length of $\text{Cs}_3\text{Sb}_2\text{X}_9$; Figure S4: Optical properties are calculated by HSE06 functional for $\text{Cs}_3\text{Sb}_2\text{Cl}_9$ (a), $\text{Cs}_3\text{Sb}_2\text{Br}_9$ (b), and $\text{Cs}_3\text{Sb}_2\text{I}_9$ (c); Table S6: Integrating absorption coefficient of $\text{Cs}_3\text{Sb}_2\text{X}_9$ calculated using HSE06.

Author Contributions: Conceptualization, Y.W., J.L. and H.M.; theoretical calculation, Y.W., G.X., M.Z., D.W. and C.C.; writing-original draft preparation, Y.W., C.C. and H.M.; writing-review and editing, Y.W., D.W., H.M. and J.L.; supervision, funding acquisition, J.L., C.C. and H.M. All authors have read and agreed to the published version of the manuscript.

Funding: This work was funded by the National Natural Science Foundation of China (NFSC) (grant No. 11904212). This work also received the financial support from by the project ZR2020MA081, ZR2019MA037 and ZR2018BA031 supported by Shandong Provincial Nature Science Foundation and the Research Leader Program of Jinan Science and Technology Bureau (2019GXRC061).

Institutional Review Board Statement: Not applicable.

Informed Consent Statement: Not applicable.

Data Availability Statement: Data are contained within the article and Supplementary materials.

Conflicts of Interest: The authors declare no conflict of interest.

References

1. Wang, A.; Guo, Y.; Zhou, Z.; Niu, X.; Wang, Y.; Muhammad, F.; Li, H.; Zhang, T.; Wang, J.; Nie, S.; et al. Aqueous acid-based synthesis of lead-free tin halide perovskites with near-unity photoluminescence quantum efficiency. *Chem. Sci.* **2019**, *10*, 4573–4579. [[CrossRef](#)] [[PubMed](#)]
2. Wang, X.D.; Miao, N.H.; Liao, J.F.; Li, W.Q.; Xie, Y.; Chen, J.; Sun, Z.M.; Chen, H.Y.; Kuang, D.B. The top-down synthesis of single-layered $\text{Cs}_4\text{CuSb}_2\text{Cl}_{12}$ halide perovskite nanocrystals for photoelectrochemical application. *Nanoscale* **2019**, *11*, 5180–5187. [[CrossRef](#)] [[PubMed](#)]
3. Laska, M.; Krzemińska, Z.; Kluczyk-Korch, K.; Schaadt, D.; Popkoa, E.; Jacak, W.A.; Jacak, J.E. Metallization of solar cells, exciton channel of plasmon photovoltaic effect in perovskite cells. *Nano Energy* **2020**, *75*, 104751. [[CrossRef](#)]
4. McCall, K.M.; Liu, Z.; Trimarchi, G.; Stoumpos, C.C.; Lin, W.; He, Y.; Hadar, I.; Kanatzidis, M.G.; Wessels, B.W. α -Particle detection and charge transport characteristics in the $\text{A}_3\text{M}_2\text{I}_9$ defect perovskites ($\text{A} = \text{Cs}, \text{Rb}; \text{M} = \text{Bi}, \text{Sb}$). *ACS Photonics* **2018**, *5*, 3748–3762. [[CrossRef](#)]
5. Wong, A.B.; Lai, M.; Eaton, S.W.; Yu, Y.; Lin, E.; Dou, L.; Fu, A.; Yang, P. Growth and anion exchange conversion of $\text{CH}_3\text{NH}_3\text{PbX}_3$ nanorod arrays for light-emitting diodes. *Nano Lett.* **2015**, *15*, 5519–5524. [[CrossRef](#)] [[PubMed](#)]

6. Chen, Y.S.; Manser, J.S.; Kamat, P.V. All solution-processed lead halide perovskite-BiVO₄ tandem assembly for photolytic solar fuels production. *J. Am. Chem. Soc.* **2015**, *137*, 974–981. [[CrossRef](#)]
7. Swarnkar, A.; Marshall, A.R.; Sanehira, E.M.; Chernomordik, B.D.; Moore, D.T.; Christians, J.A.; Chakrabarti, T.; Luther, J.M. Quantum dot-induced phase stabilization of α -CsPbI₃ perovskite for high-efficiency photovoltaics. *Science* **2016**, *354*, 92–95. [[CrossRef](#)]
8. Singh, A.; Lai, P.T.; Mohapatra, A.; Chen, C.Y.; Lin, H.W.; Lu, Y.J.; Chu, C.W. Panchromatic heterojunction solar cells for Pb-free all-inorganic antimony based perovskite. *Chem. Eng. J.* **2021**, *419*, 129424. [[CrossRef](#)]
9. Shil, S.K.; Wang, F.; Lai, Z.; Meng, Y.; Wang, Y.; Zhao, D.; Hossain, M.K.; Egbo, K.O.; Wang, Y.; Yu, K.M.; et al. Crystalline all-inorganic lead-free Cs₃Sb₂I₉ perovskite microplates with ultra-fast photoconductive response and robust thermal stability. *Nano Res.* **2021**, *14*, 4116–4124. [[CrossRef](#)]
10. Hiltunen, A.; Lamminen, N.; Salonen, H.; Liu, M.; Vivo, P. Efficiency improvement for perovskite-inspired Cs₃Sb₂I₉ solar cells using P3HT as the hole transport material. *Sustain. Energ. Fuels* **2022**, *6*, 217–222. [[CrossRef](#)]
11. Sachchidanand; Garg, V.; Kumar, A.; Sharma, P. Numerical simulation of novel lead-free Cs₃Sb₂Br₉ absorber-based highly efficient perovskite solar cell. *Opt. Mater.* **2021**, *122*, 111715. [[CrossRef](#)]
12. Singh, A.; Chiu, N.C.; Boopathi, K.M.; Lu, Y.J.; Mohapatra, A.; Li, G.; Chen, Y.F.; Guo, T.F.; Chu, C.W. Lead-free antimony-based light-emitting diodes through the vapor-anion-exchange method. *ACS Appl. Mater. Interfaces* **2019**, *11*, 35088–35094. [[CrossRef](#)]
13. Din, U.K.N.; Mohamed, M.A.; Salleh, M.M.; Aziz, T.H.T. Effect of temperature on the formation of highly crystalline lead-free perovskite Cs₃Sb₂Br₉ hexagonal microdisks. *J. Mater. Sci. Mater. Electron.* **2022**, *33*, 13625–13633. [[CrossRef](#)]
14. Jacak, J.E.; Jacak, W.A. Routes for metallization of perovskite solar cells. *Materials* **2022**, *15*, 2254. [[CrossRef](#)] [[PubMed](#)]
15. Kim, S.Y.; Yun, Y.; Shin, S.; Lee, J.H.; Heo, Y.W.; Lee, S. Wide range tuning of band gap energy of A₃B₂X₉ perovskite-like halides. *Scripta Mater.* **2019**, *166*, 107–111. [[CrossRef](#)]
16. Gu, J.; Yan, G.; Lian, Y.; Mu, Q.; Jin, H.; Zhang, Z.; Deng, Z.; Peng, Y. Bandgap engineering of a lead-free defect perovskite Cs₃Bi₂I₉ through trivalent doping of Ru³⁺. *RSC Adv.* **2018**, *8*, 25802–25807. [[CrossRef](#)]
17. Wu, L.; Dong, Z.; Zhang, L.; Liu, C.; Wang, K.; Zou, B. High-pressure band-gap engineering and metallization in the perovskite derivative Cs₃Sb₂I₉. *ChemSusChem* **2019**, *12*, 3971–3976. [[CrossRef](#)]
18. Dai, G.; Wang, L.; Cheng, S.J.; Chen, Y.; Liu, X.; Deng, L.G.; Zhong, H.Z. Perovskite quantum dots based optical fabry–perot pressure sensor. *ACS Photonics* **2020**, *7*, 2390–2394. [[CrossRef](#)]
19. Geng, T.; Ma, Z.; Chen, Y.; Cao, Y.; Lv, P.; Li, N.; Xiao, G. Bandgap engineering in two-dimensional halide perovskite Cs₃Sb₂I₉ nanocrystals under pressure. *Nanoscale* **2020**, *12*, 1425–1431. [[CrossRef](#)]
20. Blochl, P.E. Projector augmented-wave method. *Phys. Rev. B* **1994**, *50*, 17953–17979. [[CrossRef](#)]
21. Kresse, G.; Furthmüller, J. Efficient iterative schemes for ab initio total-energy calculations using a plane-wave basis set. *Phys. Rev. B* **1996**, *54*, 11169. [[CrossRef](#)] [[PubMed](#)]
22. Janoschek, R. On the relation between hartree-fock and maximum overlap molecular orbitals. *Z. Naturforsch Sect. A* **1977**, *32*, 1188–1189. [[CrossRef](#)]
23. Perdew, J.P.; Burke, K.; Ernzerhof, M. Generalized gradient approximation made simple. *Phys. Rev. Lett.* **1996**, *77*, 3865. [[CrossRef](#)] [[PubMed](#)]
24. Singh, A.; Boopathi, K.M.; Mohapatra, A.; Chen, Y.F.; Li, G.; Chu, C.W. Photovoltaic performance of vapor-assisted solution-processed layer polymorph of Cs₃Sb₂I₉. *ACS Appl. Mater. Interfaces* **2018**, *10*, 2566–2573. [[CrossRef](#)]
25. Wyckoff, R.W.G. The Structure of Crystals. *Interscience* **1951**, *3*, 478.
26. Kun, S.V.; Lazarev, V.B.; Voroshilov, Y.V.; Peresh, E.Y.; Kun, A.V. Phase equilibria in RbBr -Sb(Bi)Br₃ systems and crystal structures of compounds of the type A₃B₂C₉ (A(I)-Rb,Cs; B(V)-Sb,Bi; C(VII)-Br,I). *Izvestiya Akademii Nauk SSSR Neorganicheskie Materialy* **1993**, *29*, 410–413.
27. Rakcheeva, A.V.; Novikova, M.S.; Zaitsev, A.I.; Lubman, G.U. Perovskite-like modification of Cs₃Sb₂I₉ as a member of the OD family A₃B₂X₉. *Zhurnal Strukturnoi Khimii* **1999**, *40*, 705–715.
28. Liu, Y.L.; Yang, C.L.; Wang, M.S.; Ma, X.G.; Yi, Y.G. Theoretical insight into the optoelectronic properties of lead-free perovskite derivatives of Cs₃Sb₂X₉ (X = Cl, Br, I). *J. Mater. Sci.* **2019**, *54*, 4732–4741. [[CrossRef](#)]
29. Momma, K.; Izumi, F. VESTA 3 for three-dimensional visualization of crystal, volumetric and morphology data. *J. Appl. Cryst.* **2011**, *44*, 1272–1276. [[CrossRef](#)]
30. Jacobs, R.; Luo, G.; Morgan, D. Materials discovery of stable and non-toxic halide perovskite materials for high-efficiency solar cells. *Adv. Funct. Mater.* **2019**, *29*, 1804354. [[CrossRef](#)]
31. Pradhan, A.; Sahoo, S.C.; Sahu, A.K.; Samal, S.L. Effect of Bi substitution on Cs₃Sb₂Cl₉: Structural phase transition and band gap engineering. *Cryst. Growth Des.* **2020**, *20*, 3386–3395. [[CrossRef](#)]
32. Wang, X.; Ali, N.; Bi, G.; Wang, Y.; Shen, Q.; Rahimi-Iman, A.; Wu, H. Lead-free antimony halide perovskite with heterovalent Mn²⁺ doping. *Inorg. Chem.* **2020**, *59*, 15289–15294. [[CrossRef](#)] [[PubMed](#)]
33. Saparov, B.; Hong, F.; Sun, J.P.; Duan, H.S.; Meng, W.; Cameron, S.; Hill, I.G.; Yan, Y.; Mitzi, D.B. Thin-film preparation and characterization of Cs₃Sb₂I₉: A lead-free layered perovskite semiconductor. *Chem. Mater.* **2015**, *27*, 5622–5632. [[CrossRef](#)]
34. Molla, M.R.; Saiduzzaman, M.; Asif, T.I.; Dujana, W.A.; Hossain, K.M. Electronic phase transition from semiconducting to metallic in cubic halide CsYbCl₃ perovskite under hydrostatic pressure. *Phys. B Condens. Matter* **2022**, *630*, 413650. [[CrossRef](#)]

35. Zarabinia, N.; Rasuli, R. Electronic and optical properties of halide double-perovskites under strain: A density functional study. *Energy Sources Part A* **2021**, *43*, 2443–2455. [[CrossRef](#)]
36. Idrissi, S.; Labrim, H.; Bahmad, L.; Benyoussef, A. Study of the solar perovskite CsMBr₃ (M = Pb or Ge) photovoltaic materials: Band-gap engineering. *Solid State Sci.* **2021**, *118*, 106679. [[CrossRef](#)]
37. Islam, J.; Hossain, A. Semiconducting to metallic transition with outstanding optoelectronic properties of CsSnCl₃ perovskite under pressure. *Sci. Rep.* **2020**, *10*, 14391. [[CrossRef](#)]
38. Kong, L.; Liu, G.; Gong, J.; Hu, Q.; Schaller, R.D.; Dera, P.; Zhang, D.; Liu, Z.; Yang, W.; Zhu, K.; et al. Simultaneous band-gap narrowing and carrier-lifetime prolongation of organic-inorganic trihalide perovskites. *Proc. Natl. Acad. Sci. USA* **2016**, *113*, 8910–8915. [[CrossRef](#)]
39. Xiang, G.; Wu, Y.; Zhang, M.; Cheng, C.; Leng, J.; Ma, H. Dimension-dependent bandgap narrowing and metallization in lead-free halide perovskite Cs₃Bi₂X₉ (X = I, Br, and Cl) under high pressure. *Nanomaterials* **2021**, *11*, 2712. [[CrossRef](#)]
40. Xiang, G.; Wu, Y.; Li, Y.; Cheng, C.; Leng, J.; Ma, H. Structural and optoelectronic properties of two-dimensional ruddlesden–popper hybrid perovskite CsSnBr₃. *Nanomaterials* **2021**, *11*, 2119. [[CrossRef](#)]
41. Noor, N.A.; Mahmood, Q.; Rashid, M.; Haq, B.; Laref, A. The pressure-induced mechanical and optoelectronic behavior of cubic perovskite PbSnO₃ via ab-initio investigations. *Ceram. Int.* **2018**, *44*, 13750–13756. [[CrossRef](#)]
42. Park, B.W.; Philippe, B.; Zhang, X.; Rensmo, H.; Boschloo, G.; Johansson, E.M. Bismuth based hybrid perovskites A₃Bi₂I₉ (A: Methylammonium or cesium) for solar cell application. *Advan. Mater.* **2015**, *27*, 6806–6813. [[CrossRef](#)] [[PubMed](#)]